Supplementary Information for

High Thermoelectric Performance and Compatibility in Cu_3SbSe_4-$CuAlS_2$ Composites

Yuling Huang, Xingchen Shen, Guiwen Wang, Bin Zhang, Sikang Zheng, Chun-Chuen Yang，Xuan Hu, Shaokuan Gong, Guang Han, Guoyu Wang, Xu Lu*, Xiaoyuan Zhou*

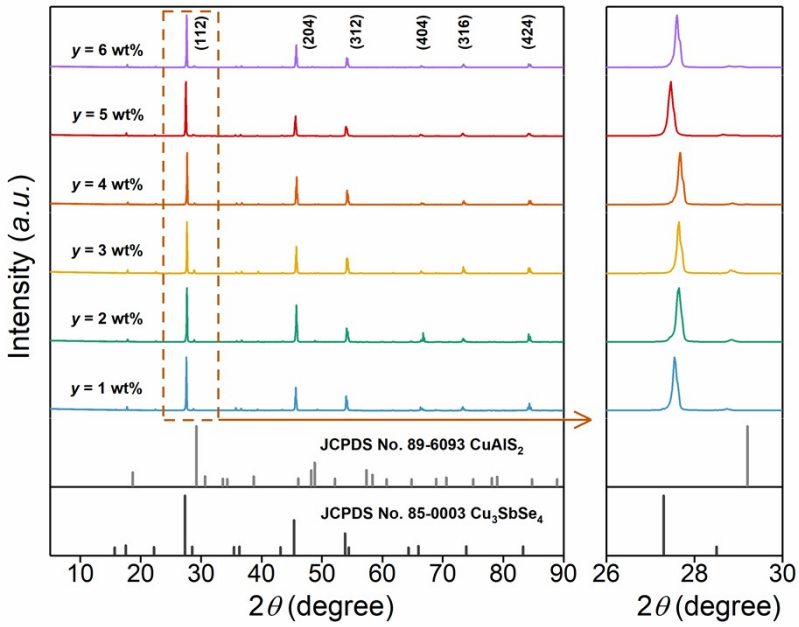

Supplementary Fig. 1 XRD patterns for the Cu_3SbSe_4-$y$$CuAlS_2$ (y = 1, 2, 3, 4, 5, and 6 wt%) samples composites with a magnified X-ray pattern of (112) plane. The majority of the diffraction peaks can be indexed to the Cu_3SbSe_4 phase with a tetragonal structure (space group I-42m).

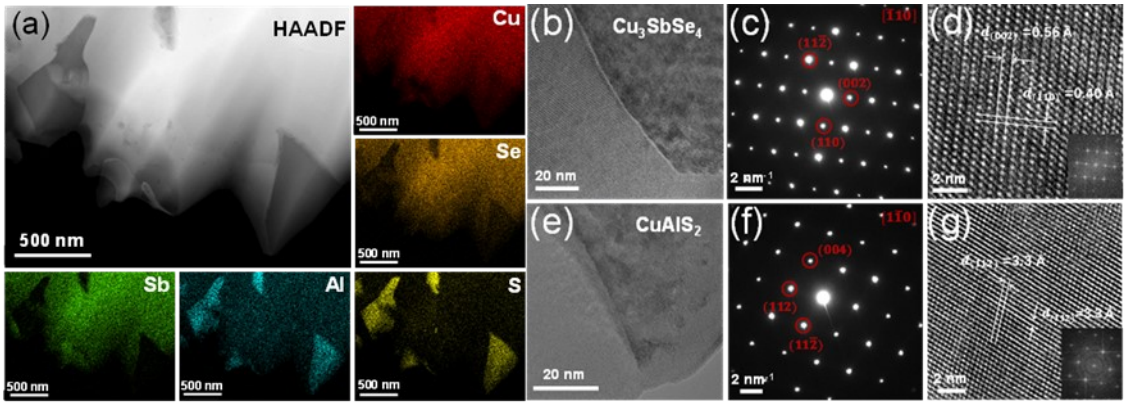

Supplementary Fig. 2-1 TEM analysis of the Cu_3SbSe_4-5 wt% $CuAlS_2$ sample. (**a**) HAADF STEM image of the matrix and $CuAlS_2$ precipitates. The corresponding EDS mappings of Cu, Sb, Se, Al and S are on the right-hand side and bottom, which reveal

formation of $CuAlS_2$ precipitates. (**b**) TEM image of the matrix with (**c**) corresponding selected area electron diffraction (SAED) pattern and (**d**) high-resolution TEM (HRTEM) image along $[\bar{1}10]$ zone axis. (**e**) TEM image of the precipitate with (**f**) corresponding SAED pattern and (**g**) HRTEM image along $[1\bar{1}0]$ zone axis.

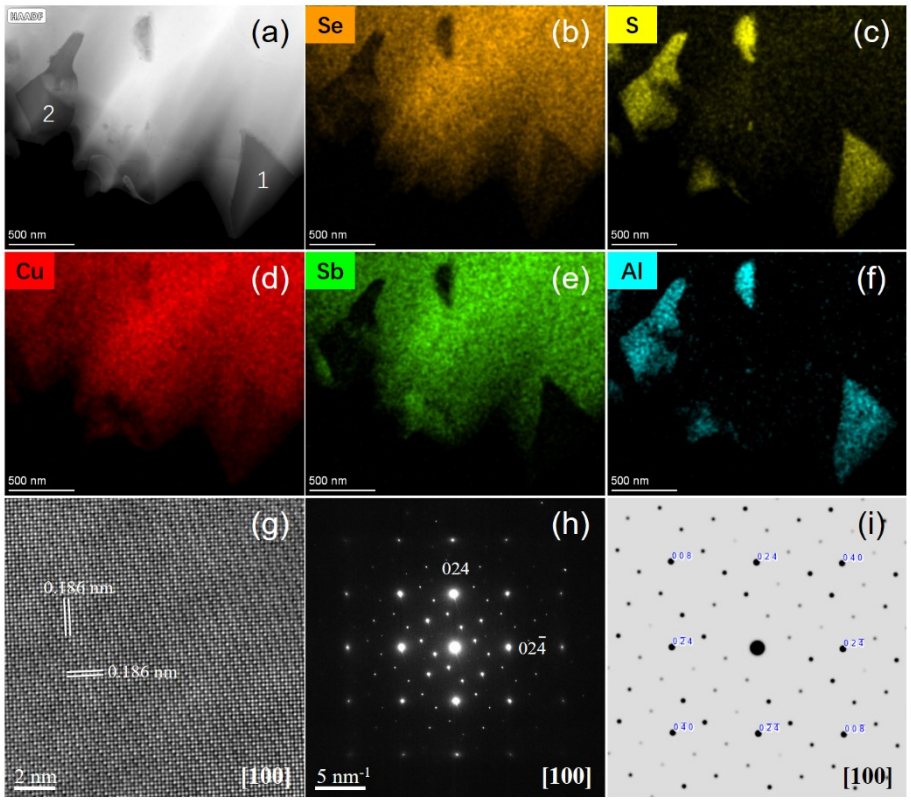

Supplementary Fig. 2-2 EDX mapping, HRTEM image and SAED pattern of precipitation.

Supplementary Table 1 Chemical composition of the precipitations.

Regions in (a)	**1**	**2**
Element	Atomic percentage %	
Cu	25.21	29.02
Al	22.22	22.20
Sb	0.66	0.93
Se	18.16	13.05
S	33.75	34.80

The precipitates were identified as $CuAlS_2$ by chemical composition (EDX) and SAED pattern with HRTEM image.

1) Chemical identification: As shown in Supplementary Fig. 2-2, the precipitates (with dimmer contrast) are rich of Al and S, but Cu is still presented only with slight deficiency. Supplementary Table 1 shows the chemical composition of 1 and 2 regions in Supplementary Fig. 2-2a, which demonstrate a chemical composition close to $CuAl(S+Se)_2$.
2) Structure analysis: The SAED pattern (Supplementary Fig. 2-2h) is well consistent with the simulated pattern (Supplementary Fig. 2-2i) of $CuAlS_2$. The lattice spacing of 0.186 nm in the corresponding HRTEM image can be well assigned to the {024} fringes of $CuAlS_2$.

In conclusion, well consistency of chemical composition and structure is sufficient to support the precipitates are $CuAlS_2$.

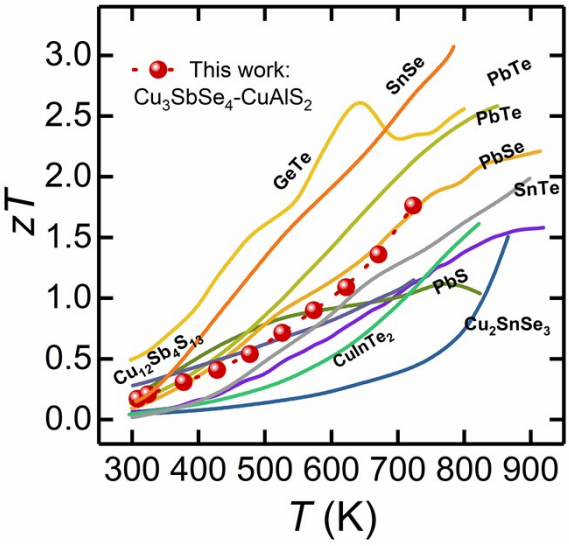

Supplementary Fig. 3 Temperature-dependent figure of merit zT for Cu_3SbSe_4-5 wt% $CuAlS_2$ with a comparison to that of known state-of-art thermoelectric performance values for *p*-type Pb based chalcogenides[1–4], GeTe[5], SnTe[6], SnSe[7] Cu-based chalcogenides[8–10].

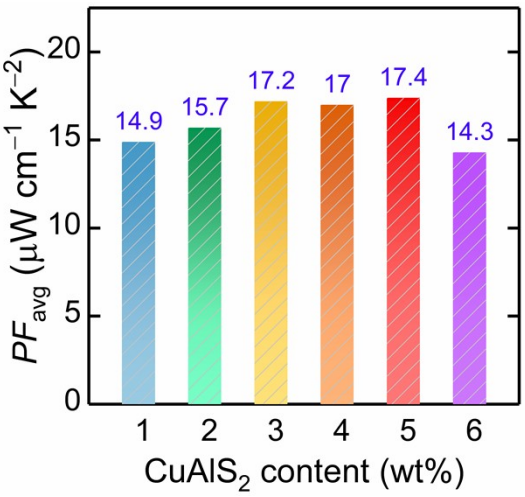

Supplementary Fig. 4 Average power factors (PF_{avg}) within working temperature for Cu_3SbSe_4-$y$$CuAlS_2$ (y = 1, 2, 3, 4, 5, and 6 wt%) samples.

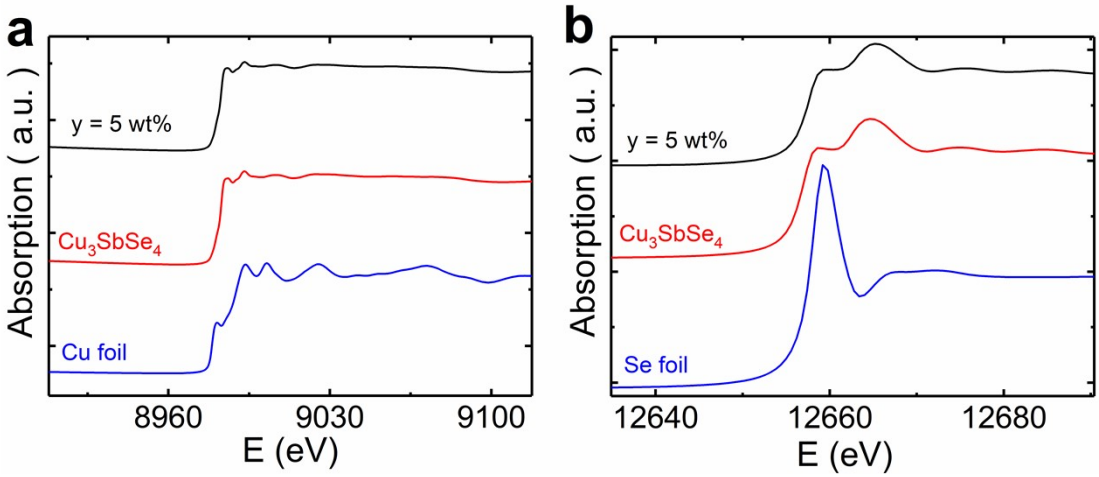

Supplementary Fig. 5 Extended x-ray absorption fine structure (EXAFS) oscillation of the K-edge of (**a**) Cu and (**b**) Se obtained for pristine Cu_3SbSe_4 and Cu_3SbSe_4-5 wt% $CuAlS_2$.

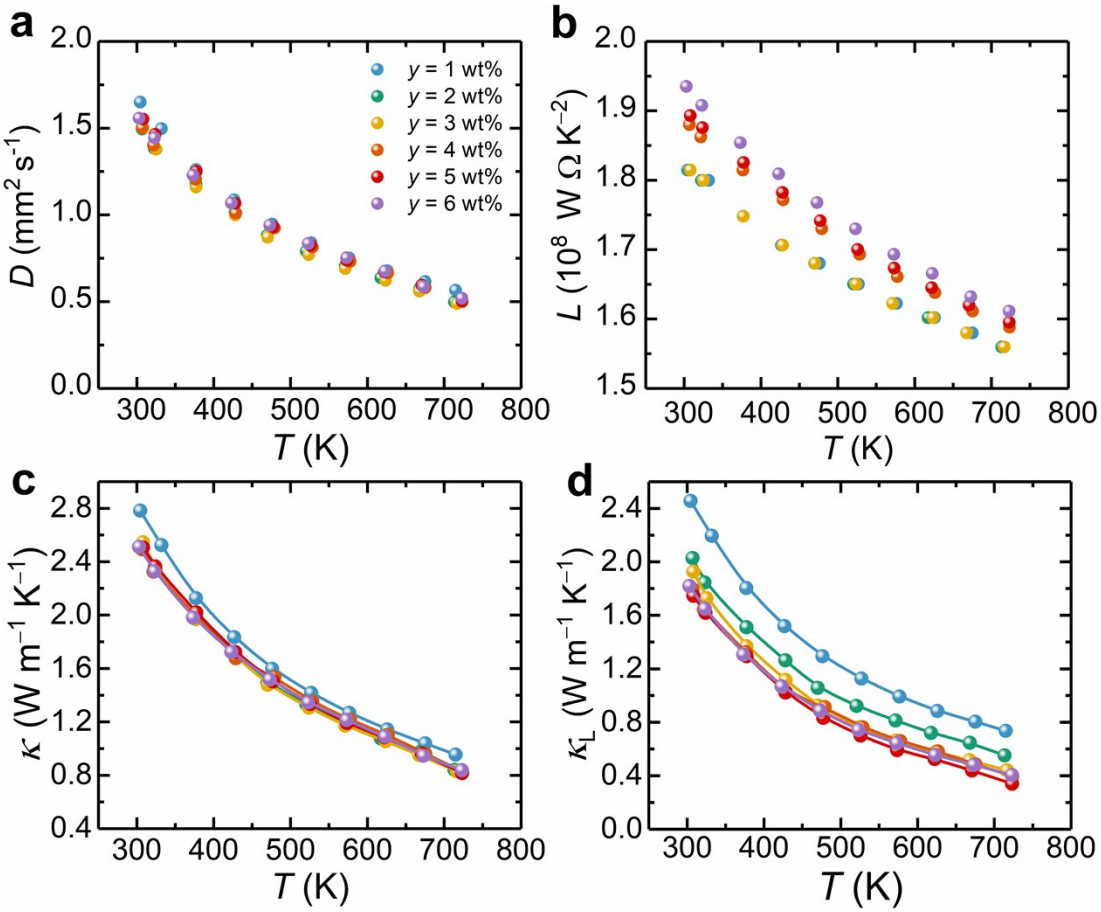

Supplementary Fig. 6 Temperature dependences of (**a**) thermal diffusive D, (**b**) Lorentz constant L, (**c**) total thermal conductivity κ and (**d**) lattice thermal conductivity κ_L for Cu_3SbSe_4-yCuAlS$_2$ (y = 1, 2, 3, 4, 5, and 6 wt%) samples.

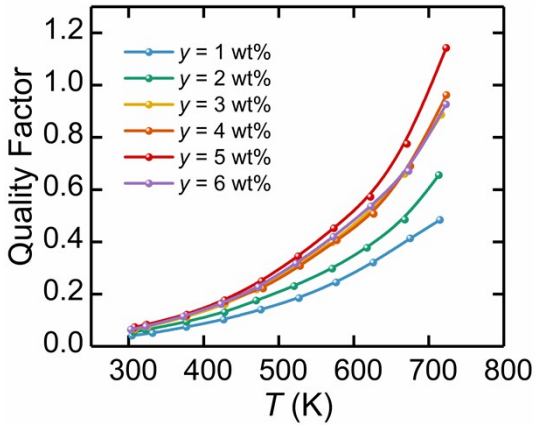

Supplementary Fig. 7 Material quality factor analysis. Quality factor **B** as a function of temperature. The composite sample with y = 5 wt% exhibits a high **B** value close to 1.2 at 723 K.

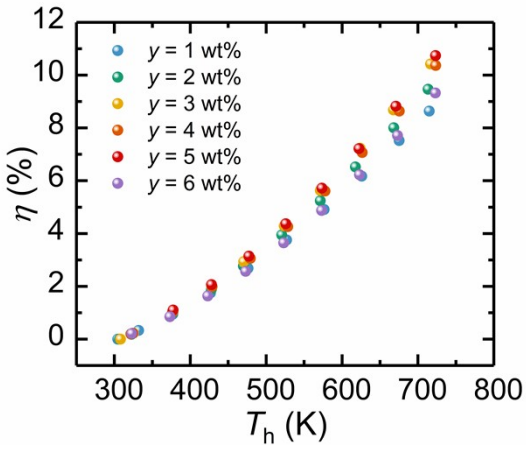

Supplementary Fig. 8 The predicted conversion efficiency of Cu_3SbSe_4-$y$$CuAlS_2$ (y = 1, 2, 3, 4, 5, and 6 wt%) as a function of hot-side temperature T_h.

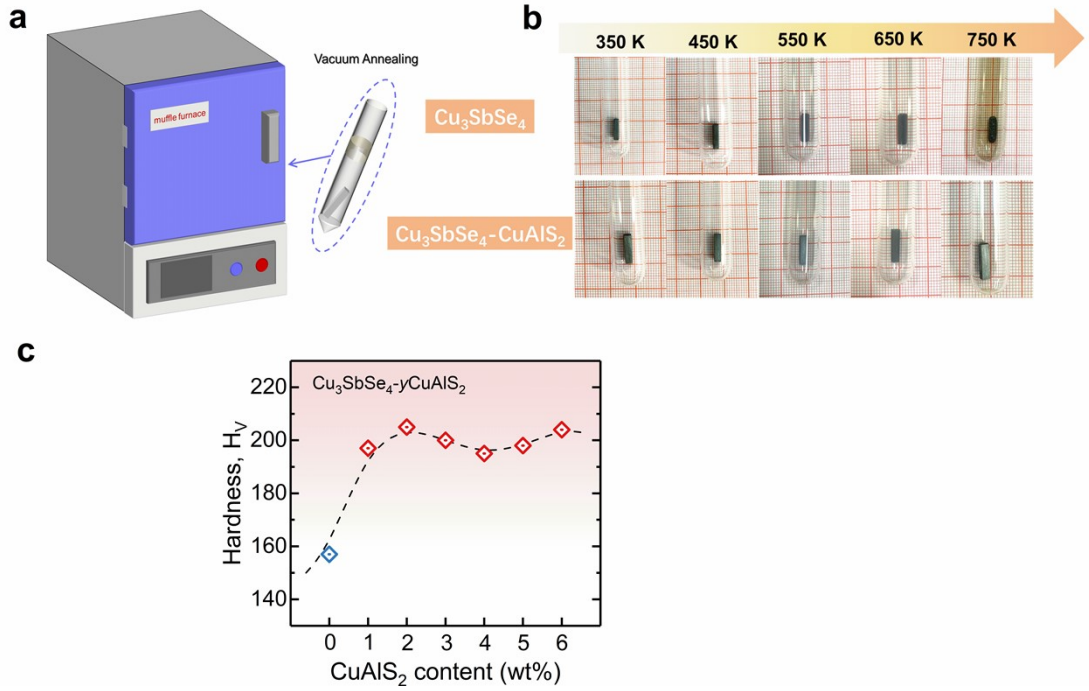

Supplementary Fig. 9 Thermal stability evaluation of Cu_3SbSe_4-$y$$CuAlS_2$ (y = 0−6 wt%) composites. (**a**) Schematic illustration of the heating apparatus to evaluate thermal stability of samples. (**b**) Photographs of Cu_3SbSe_4 and Cu_3SbSe_4-$CuAlS_2$ bulk samples annealed in the quartz tubes for 12 h at different temperatures. (**c**) Vickers hardness values of the samples at room temperature.

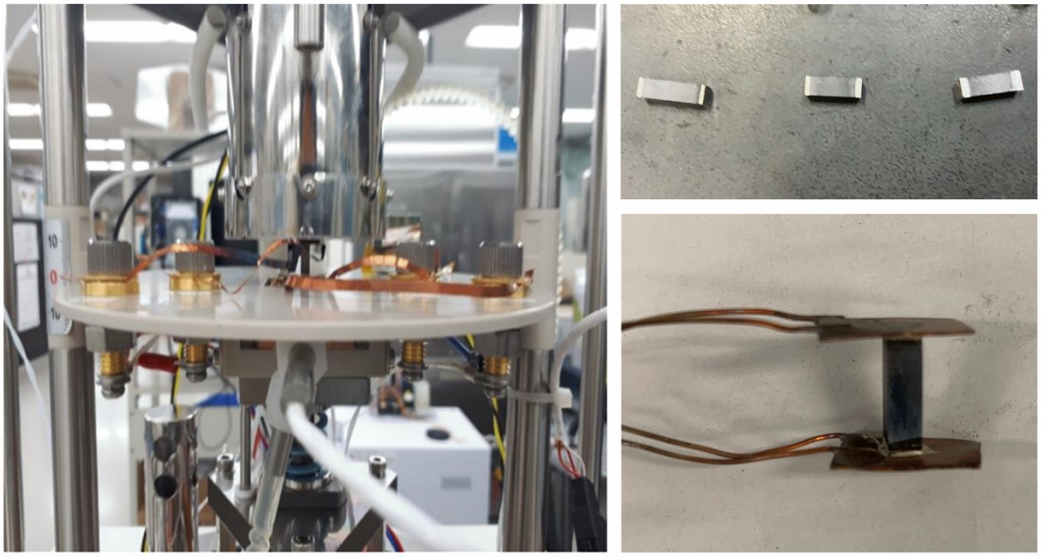

Supplementary Fig. 10 Mini-PEM for efficiency measurement of Cu_3SbSe_4-5 wt% $CuAlS_2$ single-leg device. The photos on the right are the fabricated thermoelectric single-leg. The obtained bulks were cut into a block with dimensions of 3 mm × 3 mm × 10 mm. The cold and hot sides of single-leg devices were soldered to Cu plates using Ag-based solder.

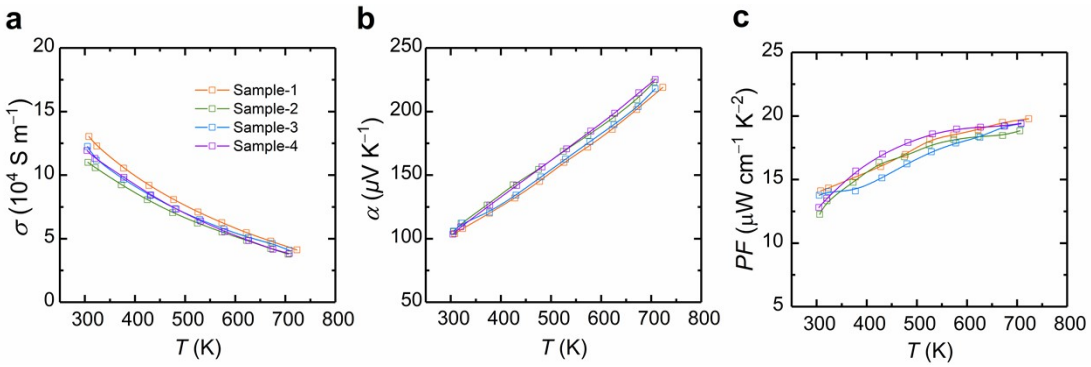

Supplementary Fig. 11 The reproducibility of electrical properties for Cu_3SbSe_4-5 wt% $CuAlS_2$. Temperature dependence of (**a**) conductivity σ, (**b**) Seebeck coefficient α and (**c**) power factor PF

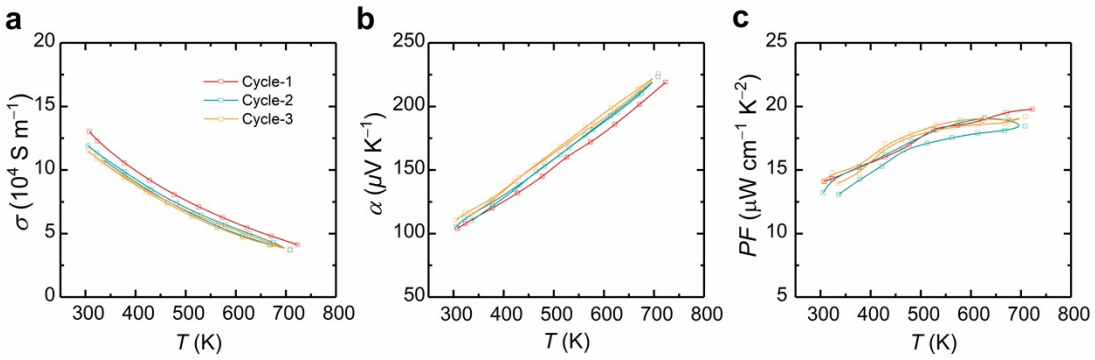

Supplementary Fig. 12 Electrical transport properties measurement for Cu_3SbSe_4-5 wt% $CuAlS_2$. Temperature dependence of (**a**) conductivity σ, (**b**) Seebeck coefficient α and (**c**) power factor *PF* under several thermal cycles.

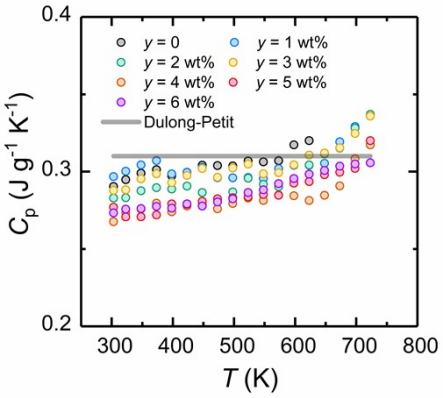

Supplementary Fig. 13 Temperature dependent specific heat capacity (C_p) for Cu_3SbSe_4-yCuAlS$_2$ (y = 1, 2, 3, 4, 5 and 6 wt%) samples.

As suggested by the literature[11], heat capacity measurement is the most challenging task among the measurements of all the thermoelectric parameters. For complex materials with similar chemical compositions, the fluctuation of data due to system error may lead to unreliable conclusion in thermal conductivity. In this case, it is safe to use Dulong-Petit value here in this study.

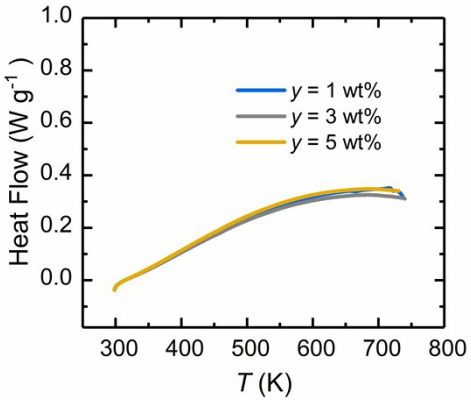

Supplementary Fig. 14 Heat flow for Cu_3SbSe_4-yCuAlS$_2$ (y = 1, 3 and 5 wt%) samples.

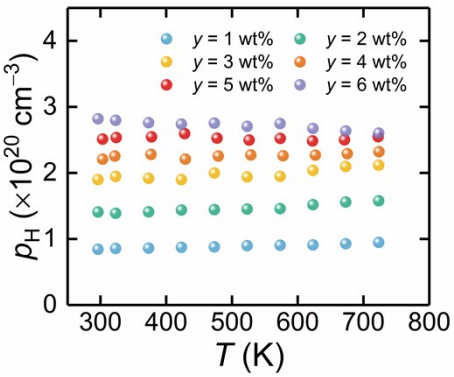

Supplementary Fig. 15 Hall carrier concentration of Cu_3SbSe_4-yCuAlS$_2$ (y = 1−6 wt%) samples as a function of temperature.

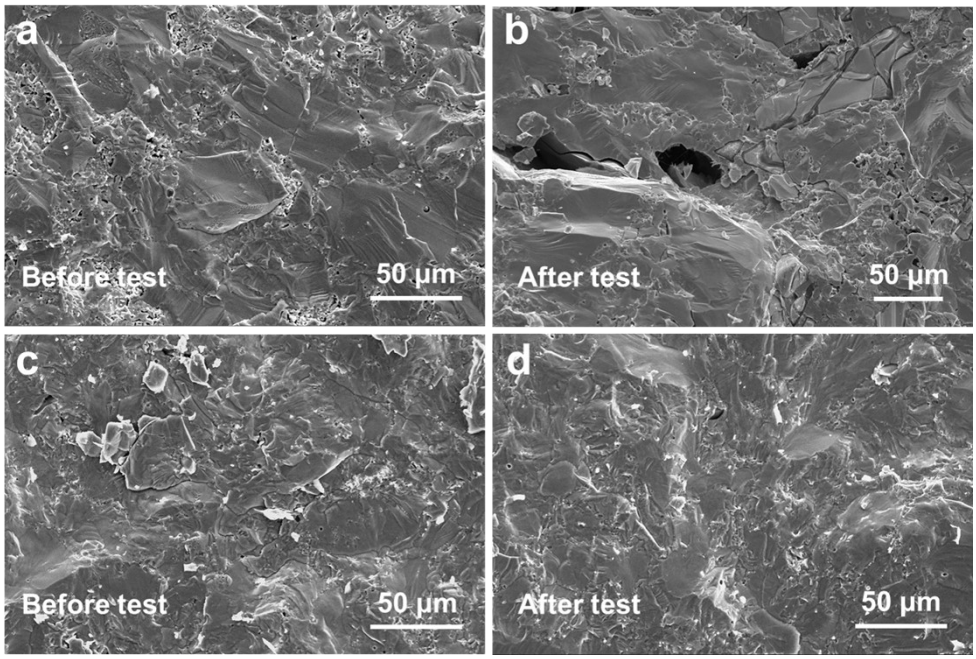

Supplementary Fig. 16 SEM images of the fracture surfaces of (a) before test and (b) after test for Cu_3SbSe_4 and (c) before test and (d) after test for Cu_3SbSe_4-5 wt% $CuAlS_2$ bulk materials.

Supplementary Table 2 The density (ρ) of Cu_3SbSe_4-yCuAlS$_2$ (y = 1−6 wt%) composites.

Samples	ρ(g cm^{-3})	Theoretical density (g cm^{-3})	Relative density (%)
y = 1 wt%	5.732	5.64	0.981
y = 2 wt%	5.695	5.56	0.971
y = 3 wt%	5.659	5.57	0.977
y = 4 wt%	5.623	5.53	0.974
y = 5 wt%	5.587	5.51	0.974
y = 6 wt%	5.552	5.47	0.971

Density of state effective mass and Pisarenko relationship calculation: We have calculated the following equations by using single parabolic band (SPB) model based on the acoustic phonon scattering mechanism[12]. The Seebeck coefficient α is given by:

$$\alpha(\zeta) = \frac{k_B}{e}\left[\frac{\left(r+\frac{5}{2}\right)F_{\left(r+\frac{3}{2}\right)}(\zeta)}{\left(r+\frac{3}{2}\right)F_{\left(r+\frac{1}{2}\right)}(\zeta)} - \zeta\right] \#(S1)$$

The hole concentration p_H is given by:

$$p_H = \frac{\left(2m^* k_B T\right)^{\frac{3}{2}}\left(r+\frac{3}{2}\right)^2 F_{\left(r+\frac{1}{2}\right)}^{2}(\zeta)}{3\pi^2\hbar^3 \left(2r+\frac{3}{2}\right)F_{\left(2r+\frac{1}{2}\right)}(\zeta)} = \frac{1}{eR_H} \#(S2)$$

The Fermi integral is given by:

$$F_x(\zeta) = \int_0^\infty \frac{\varepsilon^x}{1+\exp(\varepsilon-\zeta)} d\varepsilon \#(S3)$$

In the equations above, ζ is the reduced Fermi level, k_B is the Boltzmann constant, e is electron charge, r is the scattering factor, m^* is the density of state effective mass, $\hbar$ is the reduced Planck constant.

Lorentz constant calculation: The total thermal conductivity of thermoelectric materials can be written as $\kappa = \kappa_e + \kappa_L$, where κ_e and κ_L are the electronic thermal conductivity and lattice thermal conductivity, respectively. Therefore, the κ_L can be obtained by subtracting the κ_e from the total thermal conductivity. According to Wiedemann-Franz law: $\kappa_e = L\sigma T$, where L, σ, and T are the Lorentz constant, electrical conductivity and absolute temperature, respectively. The number of L is estimated based on the SPB model[13]:

$$L = 1.5 + exp\left(-\frac{|\alpha|}{116}\right) \#S4$$

where L is in 10^{-8} W Ω K^{-2} and α is in μV/K. And the obtained L, κ_L are shown in Supplementary Fig. 6.

Thermoelectric power generation efficiency: The device efficiency η is calculated by:

$$\eta = \frac{P}{Q} \times 100\% \#S5$$

The output power is calculated by:

$$P = IV_{out}$$

where Q, I and V_{out} are the heat flow per unit time, the current in the circuit and the load voltage, respectively.

Weighted mobility and quality factor calculation: Here the weighted mobility μ_{w} is used to evaluate the intrinsic electrical transport properties, which is defined as:

$$\mu_w = \frac{3h^3\sigma}{8\pi e\left(2m_e k_B T\right)^{\frac{3}{2}}}\left[\frac{exp\left[\frac{|\alpha|}{\frac{k_B}{e}} - 2\right]}{1 + exp\left[-5\left(\frac{|S|}{\frac{k_B}{e}} - 1\right)\right]} + \frac{\frac{3\,|\alpha|}{\pi^2 \frac{k_B}{e}}}{1 + exp\left[5\left(\frac{|\alpha|}{\frac{k_B}{e}} - 1\right)\right]}\right] \#S6$$

And the quality factor B can be calculated by:

$$B = \left(\frac{k_B}{e}\right)^2 \frac{8\pi e\left(2m_e k_B T\right)^{\frac{3}{2}} \mu_w}{3h^3 \quad \kappa_L} T \#S7$$

References

1 Y. X. Wu, Z. W. Chen, P. F. Nan, F. Xiong, S. Q. Lin, X. Y. Zhang, Y. Chen, L. D. Chen, B. H. Ge and Y. Z. Pei, 2019, *Joule* **3**, 1276–1288.

2 K. Biswas, J. Q. He, I. D. Blum, C.-I. Wu, T. P. Hogan, D. N. Seidman, V. P. Dravid and M. G. Kanatzidis, *Nature*, 2012, **489**, 414–418.

3 Y. X. Qin, T. Hong, B. C. Qin, D. Y. Wang, W. K. He, X. Gao, Y. Xiao and L.-D. Zhao, *Adv. Funct. Mater.*, 2021, **31**, 2102185.

4 B. B. Jiang, Y. Yu, H. Y. Chen, J. Cui, X. X. Liu, L. Xie and J. Q. He, *Nat. Commun.*, 2021, **12**, 3234.

5 Z. L. Bu, X. Y. Zhang, B. Shan, J. Tang, H. X. Liu, Z. W. Chen, S. Q. Lin, W. Li and Y. Z. Pei, *Sci. Adv.*, 2021, **7**, eabf2738.

6 W. Li, L. L. Zheng, B. H. Ge, S. Q. Lin, X. Y. Zhang, Z. W. Chen, Y. J. Chang and Y. Z. Pei,*Adv. Mater.*, 2017, **29**, 1605887.

7 C. J. Zhou, Y. K. Lee, Y. Yu, S. J. Byun, Z.-Z. Luo, H. Lee, B. Z. Ge, Y.-L. Lee, X. Q. Chen, J. Y. Lee, O. C. Mirédin, H. Chang, J. Im, S.-P. Cho, M. Wuttig, V. P. Dravid, M. G. Kanatzidis and I. Chung, *Nat. Mater.*, 2021, 20, 1378–1384.

8 H. W. Ming, G. F. Zhu, C. Zhu, X. Y. Qin, T. Chen, J. Zhang, D. Li, H. X. Xin and B. Jabar, *ACS Nano*, 2021, **15**, 10532–10541.

9 Y. B. Luo , J. Y. Yang , Q. H. Jiang , W. X. Li , D. Zhang , Z. W. Zhou , Y. D. Cheng , Y. Y. Ren and X. He, *Adv. Energy Mater.*, 2016, **6**, 1600007.

10 H. H. Hu, H.-L. Zhuang, Y. L. Jiang, J. L. Shi, J.-W. Li, B. W. Cai, Z. R. Han, J. Pei, B. Su, Z.-H. Ge, B.-P. Zhang and J.-F. Li, *Adv. Mater.*, 2021, **33**, 2103633.

11 Z.H. Liu, W.H. Gao, F.K. Guo, W. Cai, Q. Zhang, and J.H. Sui, Materials Lab, 2022, 1, 220003.

12 J. W. Shen, Z. W. Chen, S. Q. lin, L. L. Zheng, W. Li and Y. Z. Pei, *J. Mater. Chem. C*, 2015, **4**, 209–214.

13 H. S. Kim, Z. M. Gibbs, Y. Tang, H. Wang, and G. J. Snyder, *APL Mater.*, 2015, **3**, 041506.